remote sensing

MDPI

Article

Observed Mesoscale Wind Response to Sea Surface Temperature Patterns: Modulation by Large-Scale Physical Conditions

Lorenzo F. Davoli, Agostino N. Meroni and Claudia Pasquero *

Department of Earth and Environmental Sciences, University of Milano-Bicocca, Piazza dell'Ateneo Nuovo 1, 20126 Milan, Italy; l.davoli@campus.unimib.it (L.F.D.); agostino.meroni@unimib.it (A.N.M.)
* Correspondence: claudia.pasquero@unimib.it

Highlights

What are the main findings?

- Satellite observations confirm the control of large-scale wind speed and atmospheric stability on mesoscale SST-wind coupling.
- Observations reveal a more linear relationship between wind divergence and SST gradients and a more consistent dependence of the coupling on environmental conditions compared to reanalysis data, which show stronger nonlinearities and regional differences.

What is the implication of the main finding?

- In addition to large-scale wind and atmospheric stability, boundary layer height and the spatial scale of the SST features play a major role in modulating the coupling intensity.
- Reanalysis data show important limitations in their representation of SST-wind coupling in stable conditions, likely due to an overestimation of boundary layer depth.

Abstract

Sea surface temperature (SST) gradients modulate surface wind variability at the mesoscale O(100 km), with relevant impacts on surface fluxes, rainfall, cloudiness and storms. The dependence of the SST-wind coupling mechanisms on physical environmental conditions has been proven using global ERA5 reanalysis data, regional observations and models. However, recent literature calls for the need of an observational confirmation to overcome the limitations of numerical simulations in representing such turbulent processes. Here, we employ O(10 km) MetOp A observations of surface wind and SST to verify the dependence of the downward momentum mixing (DMM) mechanism on large-scale wind U and atmospheric stability. We propose a simple empirical model describing how the coupling intensity varies as a function of U, where we account for the role of the characteristic SST length scale LSST and the boundary layer height h in determining the balance between the advective and response timescales, and therefore the decoupling of the atmospheric response from the SST forcing due to advection. Fitting such a model to the observations, we retrieve a scaling with U that depends on the atmospheric stability, in agreement with the literature. The physical interpretation from ERA5 is confirmed, albeit relevant discrepancies emerge in stable regimes and specific regional contexts. This suggests that global numerical models are not able to properly reproduce the coupling in certain conditions, which might have important implications for air–sea fluxes.

Keywords: space-borne Earth observations; air–sea interactions; mesoscale; numerical models; scatterometers; radiometers; ASCAT; AVHRR; MetOp; ERA5; reanalysis; atmospheric instability; large-scale wind; downward momentum mixing

Academic Editors: Weimin Huang, Xi Zhang, Jinpeng Zhang and Xiaofeng Zhao

Received: 23 September 2025
Revised: 31 October 2025
Accepted: 15 November 2025
Published: 19 November 2025

Citation: Davoli, L.F.; Meroni, A.N.; Pasquero, C. Observed Mesoscale Wind Response to Sea Surface Temperature Patterns: Modulation by Large-Scale Physical Conditions. *Remote Sens.* **2025**, *17*, 3764. https://doi.org/10.3390/rs17223764

1. Introduction

Air–sea interactions play a crucial role in the transfer of heat, moisture, and momentum at the ocean-atmosphere interface. In the 1990s, monthly estimates of surface heat fluxes at 1° × 1° resolution from optical and infrared observations of clouds and microwave radiometers showed surface wind is one of the major regulators of sea surface temperature (SST) due to its role in enhancing evaporative cooling and mixing with subsurface waters [1]. These findings confirmed the leading role of the atmospheric wind in driving the ocean temperature variability at the basin scale, i.e., at scales larger than 1000 km [2].

In the last two decades, the availability of high-resolution $O(10)$ km scatterometer, radiometer and $O(100)$ m SAR satellite observations has given a strong impulse to the study of air–sea interactions at smaller scales. Since then, relevant fine-scale interactions between the ocean mixed layer, the marine atmospheric boundary layer (MABL), and the free troposphere have been observed or investigated with numerical models [2–5]. Fine-scale analyses show a predominant role of the ocean features in driving the atmospheric variability [6]. At the oceanic mesoscales, corresponding to horizontal scales of $O(100–1000)$ km and weekly to monthly timescales, SST fronts, eddies, and oceanic currents have been observed to induce a tropospheric response with important weather and climate impacts (e.g., [3,7,8]). Studies conducted over regions with strong persistent SST gradients, such as western boundary currents, highlight a strong climatological response of tropospheric wind, clouds and rainfall to sharp SST fronts [9–11], while oceanic eddies contribute substantially to the net heat exchange between the atmosphere and the ocean [12–14]. Strong SST gradients also play an important role in storm development and intensification at daily scales [15,16]. Simulations and observations of air–sea interactions at the submesoscales $O(1–100)$ km suggest a behaviour similar to that observed at the mesoscales [17–19] with notable differences related to the entanglement of different processes [20] and their strengths [21]. In particular, the systematic assessment of the intensity of such interactions and their feedback on larger scales is an active area of research [22].

Mesoscale air–sea interactions encompass various processes, usually divided into thermal (TFBs) and current (CFBs) feedbacks, which describe the influence of SST and ocean currents on the MABL. In the case of CFBs, the relative motion between the surface wind and the current generates a wind stress anomaly, increasing the momentum transfer from the ocean to the atmosphere [23,24]. As a main consequence, this mechanism acts as an "eddy killer", with relevant effects on the kinetic energy repartition in the ocean. Mesoscale currents, being mostly geostrophic, do not exhibit a relevant divergence, and therefore they only induce a response in surface wind curl, allowing for a decoupling from TFBs acting on surface wind divergence [25].

Within TFBs, the main mechanisms explaining wind-SST coupling are downward momentum mixing (DMM) [26,27] and pressure adjustment (PA) [28]. DMM consists of an increased transport of momentum from the free troposphere to the surface due to enhanced mixing when passing from colder to warmer SST. This atmospheric mixing is enhanced by the increasing heat turbulent fluxes in the transition, resulting in the deepening of the MABL due to the entrainment of free tropospheric air, which results in higher surface wind and a weaker wind at the MABL top [29]. According to the PA mechanism, a negative (positive) surface pressure anomaly develops over a warm (cold) SST anomaly due to the increased (decreased) sensible heat flux. The related pressure gradient induces a secondary circulation exhibiting surface wind convergence (divergence) over the SST anomaly. The intensity of the TFB mechanisms is usually measured with coupling coefficients, which are the linear slope of the binned scatterplot of relevant fields. For instance, for DMM, the SST gradient and the surface wind divergence are considered, whereas for PA the SST Laplacian and the surface wind divergence are analysed [2,3,7,30,31].

Studies comparing SST-wind coupling coefficients from satellite observations and from high-resolution numerical simulations show large discrepancies, both for atmospheric [25,32] and for ocean-atmosphere coupled models [33]. This can be related to the parametrisation of unresolved processes, as demonstrated by the dependence of the coupling coefficients on the choice of the MABL turbulent scheme [34,35], and indicates that models still struggle in properly representing air–sea interactions, possibly influencing long-standing biases in global models [36]. The analysis of air–sea interactions from observational data is thus useful both to characterise the processes at play and to guide the development of revised numerical schemes.

Instantaneous and daily scatterometer and radiometer observations have shown a significantly larger value of DMM coupling coefficient with respect to that obtained from multi-annual and monthly data over the Gulf Stream [3,7,37]. Similar results have been found both at the mesoscale and at the submesoscale, and they suggest that SST-wind coupling is active at very short, sub-daily timescales [17,18,38].

Regional factors also play a role in modulating the coupling intensity via different environmental properties [7,39,40], where the term "environmental" refers to the physical conditions of the atmosphere in the surroundings. For example, the coupling strength has been shown to depend on the scale of motion and on the Rossby number, as they directly affect the advective timescale and the characteristic length of the SST features [41].

Large-scale wind speed and atmospheric stability are also important drivers of daily DMM and PA coupling intensity [40]. In addition to its contribution to advection, large-scale wind is related to the free tropospheric wind, which powers DMM, while atmospheric stability regulates the development of the vertical motion, which plays a key role in both DMM and PA [39–41]. These relationships have been described starting from the analysis of numerical simulations and of global reanalysis data that present systematic biases in surface wind compared to scatterometer observations [36,42–44] and in MABL humidity, temperature and surface heat fluxes [18,45–47]. The role of the large-scale wind in modulating the coupling of the wind stress to the SST (and its differences with respect to the coupling of the wind field to the SST) has been highlighted from satellite data only at monthly time scales [48]. A corresponding analysis at daily and sub-daily scales based on remote sensing data, which is still missing, would shed new light on this fast physical air–sea interaction.

Here, our objective is twofold: (1) to provide a global observational assessment of the environmental control of large-scale wind and atmospheric instability on the intensity of the DMM coupling following Desbiolles et al. (2023) [40], and (2) to verify how much of the physical interpretation based on the reanalysis and the observational global datasets translates at the regional level, and which additional factors could be responsible for uncaptured variability of the DMM coupling emerging in regional contexts. Section 2 describes the data and methods used, while results are presented in Section 3. Section 4 is devoted to a final discussion.

2. Materials and Methods

2.1. Datasets

The observational analysis covers the period between January 2020 and October 2021, employing satellite data from the MetOp-A platform. SST data come from the Advanced Very High Resolution Radiometer (AVHRR) instrument onboard of MetOp-A, distributed as part of the ESA-CCI dataset. In particular, we make use of the L3C (Level 3 Collated) product v2.1 obtained from the Copernicus Climate Change Service (C3S) Climate Data Store (CDS) platform [49]. It consists of instantaneous skin SST observations provided as global maps, collecting all orbits on a 0.05° latitude-longitude regular grid, separated

between night-time and day-time acquisitions. The data are not available in the presence of sea ice and clouds, which strongly reduce the coverage in regions with high cloud cover and polar regions. Quality flags are attributed to the data representing their reliability depending on the known causes of uncertainties in the processing, such as dust and thin clouds. Following Merchant et al. (2019) [50], all data with a quality flag of 3 or higher are considered reliable for the computation of gradients for our analyses.

Surface wind observations consist of 10 m equivalent neutral wind estimates of the L2 coastal product derived from the MetOp-A Advanced Scatterometer (ASCAT) Climate Data Record (CDR) dataset [51]. They are available on the NASA JPL-PODAAC platform in the format of single orbit files containing instantaneous observations of the two 550 km swaths on a 12.5 km irregular grid, following the satellite track projection on the surface. The data are also quality-flagged based on their reliability, with rainfall and extremely low or high values of wind speed as the main known sources of uncertainty. We remove all the points with high uncertainty (quality flag higher than 10^5) to ensure the reliability of the analysis.

Atmospheric stability is here defined using air–sea temperature difference ($T_{air} - SST$) as a proxy [40,52], given that it regulates surface heat fluxes and therefore the buoyancy flux and air-column stability. Clearly, other factors such as moisture and subsidence influence stability but will not be considered here. Negative (positive) values of air–sea temperature differences correspond to a warm (cold) ocean heating (cooling) the overlying atmosphere, favouring (inhibiting) vertical transport due to the enhanced (reduced) surface buoyancy. At present, no satellite observations of surface air temperature provide adequate spatial coverage and resolution to be collocated with MetOp data used to compute mesoscale SST forcing and surface wind response. Consequently, to estimate the air–sea temperature difference, we employ hourly ERA5 data for 2 m air temperature and SST. ERA5 is a global reanalysis describing the atmosphere, land surface and ocean surface produced by the European Centre for Medium-Range Weather Forecasts (ECMWF) and distributed through the CDS portal [46]. The data are on a regular grid at 0.25° horizontal spacing and hourly frequency. ERA5 provides estimates of atmospheric, ocean-wave and land-surface variables, while the foundation SST field is prescribed as a boundary condition, and it is obtained from the HadISST and OSTIA L4 products with a daily update frequency [53,54]. The model also assimilates a wide set of satellite and in-situ observations, making it a reference dataset for atmospheric physics studies. In the observational analysis, using two distinct SST products is necessary to prevent inconsistencies between SST and wind fine-scale variability in MetOp instantaneous observations, as well as between SST and air temperature estimates in the calculation $T_{air} - SST$ from ERA5. Furthermore, we expect ERA5 to accurately represent large-scale atmospheric conditions, aligning well with its intended role in the analysis.

From ERA5, we also take daily fields of 10m wind, foundation SST, and 2 m air temperature to reproduce the analyses from Desbiolles et al. (2023) [40] in the time window between January 2000 and December 2021.

2.2. Data Analysis and Coupling Metrics

We aim to compute the DMM coupling coefficients as a function of the large-scale wind and the air stability defined as the air–sea temperature difference. To do so, a few pre-processing steps are needed. In the observational dataset, following the methodology of Meroni et al. (2023) [37], SST data are smoothed through a Gaussian filter with a standard deviation of 10 km to reduce the noise and remove the fine-scale variability that is not captured by the wind product, being it on a coarser grid. Wind data are interpolated on the finer SST regular grid using a bilinear interpolation. This is meant to preserve the full range of variability of SST gradients and has the effect of repeating wind divergence values over contiguous pixels. A 50 km coastal mask is applied to all datasets to remove coastal

effects such as land-sea breeze and orographic effects, and to ensure the scatterometer observations are not affected by land scattering.

An isotropic Gaussian low-pass filter is then applied to the surface wind field $\vec{u}$ to estimate its large-scale component $\vec{U}$ and, from that, the mesoscale anomaly $\vec{u'} = \vec{u} - \vec{U}$. This anomaly can be decomposed on a local Cartesian frame of reference $\{\hat{r}, \hat{s}\}$, with $\hat{r}$ being the along-$\vec{U}$ direction and $\hat{s}$ the across-$\vec{U}$ direction (positive at 90° counterclockwise to $\hat{r}$), so that

$$\vec{u'} = u'_r \cdot \hat{r} + u'_s \cdot \hat{s}, \tag{1}$$

as in [55].

The standard deviation of the Gaussian filter σ is defined differently depending on the wind field product considered. For ERA5 wind, $\sigma = 450$ km, which provides a smoothing comparable to the 1000 km Lanczos filter used in Desbiolles et al. (2023) [40]. For ASCAT wind, instead, $\sigma = 50$ km, as in Meroni et al. (2022, 2023) [37,55]. Sensitivity analyses for σ applied to both wind products ($\sigma = 225$ km for ERA5 and $\sigma = 450$ km for ASCAT) indicate that results have a negligible dependence on it, for reasons that are discussed later in the manuscript.

From the SST and u'_r fields, centred finite-difference spatial derivatives are computed to obtain the along-wind SST gradient $\partial \mathrm{SST}/\partial r$ and the along-wind divergence $\partial u'_r/\partial r$. Following Meroni et al. (2023) [37], the DMM coupling coefficient α_{DMM} is defined as the slope of the linear regression between these two fields, as in

$$\frac{\partial u'_r}{\partial r} = \alpha_{DMM} \cdot \frac{\partial \mathrm{SST}}{\partial r}. \tag{2}$$

As most of the SST gradients fall into a narrow interval corresponding to weak SST gradients, in fact sharp SST features are rare across the ocean, a weighted linear regression is applied to the uniformly binned SST gradient distribution. We define 20 bins of $\partial \mathrm{SST}/\partial r$ and for each of them we compute the mean SST gradient, the mean wind divergence, and its standard error (defined as the ratio between the standard deviation and the square root of the number of values in the bin). The standard error is used as a weight in the least-square linear regression, as in "Numerical Recipes", Equation (15.2.6) [56]. The uncertainty of each coupling coefficient is estimated through the square root of slope variance according to "Numerical Recipes", Equation (15.2.9) [56]. To increase the robustness of the regression, bins containing fewer than 100 points are excluded, and we avoid computing the regression if more than 50% of the bins are rejected in this way. This approach serves three purposes. First, uniform bins give equal relevance to the whole range of SST gradients, reducing the bias induced by the distribution of the population. Second, the systematic loss in the representation of extreme SST gradients, which occurs as the population decreases under extreme environmental conditions, is addressed not by adapting the uniform binning to the reduced range, but by progressively discarding those fixed bins that are insufficiently populated. This step ensures that, by maintaining fixed bins, the linear regression is always performed over a consistent sampling of SST gradients, thereby guaranteeing comparability across different regressions. Third, the regression emphasises the most reliable bins by weighting according to their uncertainty, reducing the potential bias introduced by comparing bins with different populations. Furthermore, cases where the coefficient of determination (R^2) of the least-squares regression falls below 0.8 are also discarded. This eliminates cases that would make the estimate of the coupling coefficients unreliable, such as cases where the slope shifts sign between positive and negative SST gradients. For each region and product, a different binning of the SST gradient distribution is defined to cover its full range. This is needed because we compare subsets with very different ranges of SST gradients, partially due to the presence or absence of sharp SST features (e.g., in

western boundary currents), and partially because of the variability of the Rossby radius of deformation with latitude, which may indirectly affect the SST gradient strength.

The methodology described above is used to compute coupling coefficients over subsets of data grouped by the values of their large-scale conditions. Classes of large-scale wind speed U range from 0 m/s to 24 m/s, with a sampling frequency of 2 m/s, while classes of air stability $T_{air} - SST$ range from -16 K to 6 K, sampled every 2 K. As the statistics of the environmental conditions and of the SST gradients are not uniform across regions, environmental classes which are poorly populated in certain regions (e.g., strongly unstable conditions in the Tropics) do not allow us to estimate their corresponding coupling coefficients.

We tested the methodologies of Meroni et al. (2023) [37] and Desbiolles et al. (2023) [40] against the methodology proposed here to evaluate its potential biases. The tests showed that the exact value of the coupling coefficient is sensitive to the precise methodology used to compute it (we obtained values 30% smaller than the one in Meroni et al. (2023) [37], and 40% larger than in Desbiolles et al. (2023) [40]), but the dependence on environmental conditions is not affected.

2.3. Regions of Interest

Regional analyses are carried out over the regions reported in Figure 1. Mid-latitude regions, namely the Gulf Stream, the Agulhas Current (including both the Retroflection and Return Current), the Malvinas-Brasilian Confluence (BMC) region, and the Kuroshio Current, are defined as in O'Neill et al. (2012) [48], and their boundaries are reported in Table S1 in the Supplementary Materials. These regions are rich in mesoscale SST features and present very sharp SST gradients, in the order of 1 K/10 km, which generate strong feedback mechanisms [8,57–59]. They are characterised by strong westerly winds and a wide range of atmospheric stability conditions, varying from marginally stable ($T_{air} - SST \sim 5$ K) to very unstable ($T_{air} - SST \sim -20$ K). Strong instability often develops during the cold season, when cold air outbreaks (CAOs) bring cold air masses from the continental plains over the Gulf Stream and the Kuroshio current [60]. Tropical areas, such as the EUREC^{4}A region near Barbados (where the EUREC^{4}A, ElUcidating the RolE of Cloud–Circulation Coupling in ClimAte, field campaign took place) [61] and the Benguela current along the coasts of Namibia and Angola, present mostly marginally unstable to marginally stable conditions ($T_{air} - SST \in [-5\text{ K}; 3\text{ K}]$), with weaker winds and milder SST gradients.

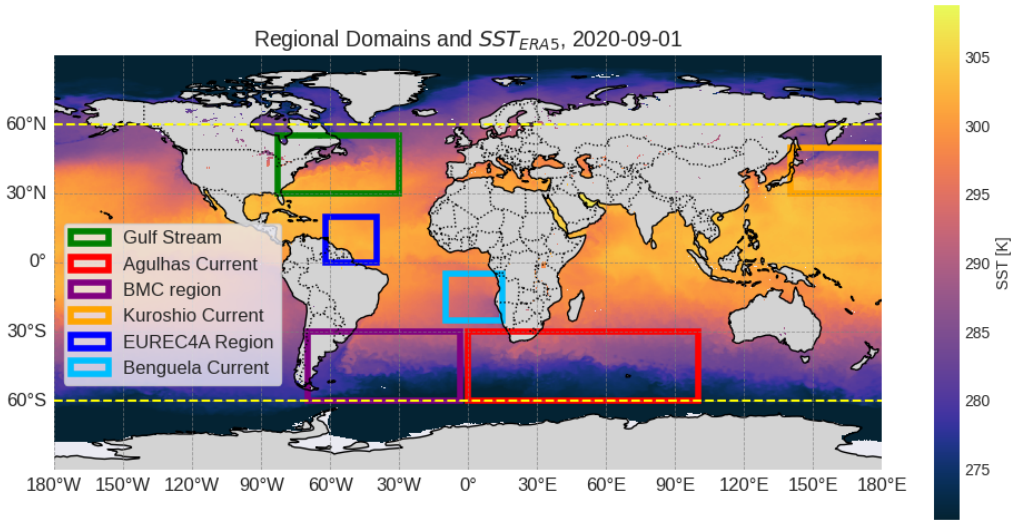

Figure 1. Domains for regional analysis and SST field on the 1 September 2020 from ERA5 (in the background). Yellow dashed lines highlight the boundaries of the global domain (between $-60°$ and 60° latitude).

Global analyses are also performed, employing data between −60° and 60° latitudes to reduce the impact of sea ice and ensure the comparability with Desbiolles et al. (2023) [40].

3. Results

3.1. Global Analysis of Coupling Dependence on Environmental Conditions

Global reanalysis data and regional observations have highlighted the dependence of the DMM coupling coefficients on environmental conditions such as large-scale wind speed, atmospheric instability and Rossby number [40,41]. Here, we present a framework to interpret those dependencies; we investigate if the same results are confirmed by global observations and if any discrepancy from the global analyses emerges at the regional level for both observational and reanalysis data. During this process, we do not aim to compare observations and reanalysis data in terms of the absolute values of their coupling coefficients, as we know that they are influenced by existing structural and methodological differences between the two products. Instead, we verify if any discrepancy emerges in the shape of the dependency of the coupling intensity on the environmental conditions.

First, we focus on the influence of U on the DMM mechanism, which shows, both for the observational and for the reanalysis datasets, an initial increase in coupling intensity followed by a peak and a subsequent decrease at larger U (Figure 2a). For ERA5, the decrease is barely visible for wind speeds exceeding 13 m/s due to the scarcity of strong winds in the reanalysis dataset. Indeed, when relaxing the condition on the minimum number of SST gradient bins from 50% to 40% of their total, a value of $\alpha_{DMM} = 0.22$ ms^{-1}K^{-1} is found for $U = 17$ m/s, thereby confirming its decreasing trend for stronger winds (see Supplementary Material, Figure S1).

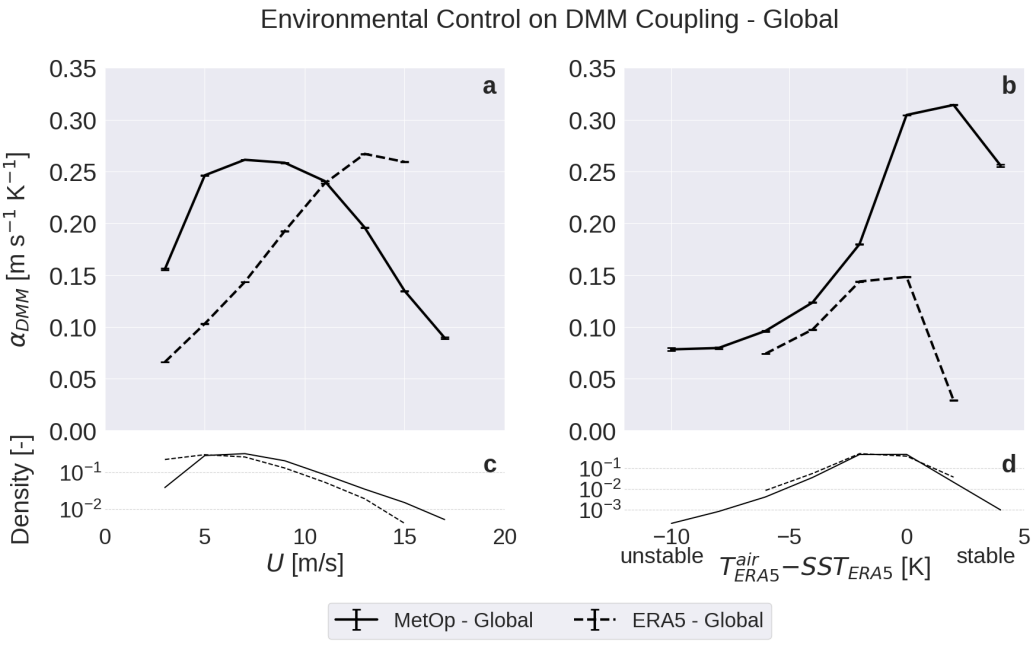

Figure 2. DMM coupling coefficient α_{DMM} as a function of large-scale surface wind speed U (**a**) and air–sea temperature difference $T_{air} - SST$ (**b**) from global MetOp observations (full line) and ERA5 data (dash line), with the corresponding density distributions (**c**,**d**) in log-scale.

To interpret the existence of a maximum in coupling coefficient for an intermediate large scale wind speed, we consider that the atmospheric response to underlying SST patterns is controlled by the ratio between two timescales [40]: the advective timescale

$$\tau_{adv} = \frac{L_{SST}}{U}, \tag{3}$$

where L_{SST} is a representative length scale of the SST feature, and the time scale of the DMM response

$$\tau_{res} \propto h, \tag{4}$$

considered to be proportional to the boundary layer height h. Whenever the response time scale is short compared to the advective time scale, the imprint of the SST patterns will manifest in the near-surface winds. Conversely, for long τ_{res} compared to τ_{adv}, the boundary layer properties will not have the time to fully adjust to the underlying SST before the air moves away from the SST feature, and the response will be weak. In relation to the environmental conditions introduced above, we note that the boundary layer height depends on air column stability and on wind speed [8,62,63], and that the spatial scale of the SST structures is related to the Rossby number.

To discuss the dependence of the coupling coefficient α_{DMM} solely on the large-scale wind U, as shown in Figure 2a, we assume, as a first approximation, that h is independent of U, and therefore we can treat τ_{res} as constant. At low U, the advective timescale is large, resulting in $\tau_{res} \ll \tau_{adv}$. For increasing large-scale wind U, we postulate that also the free-tropospheric wind increases. Thus, the enhanced mixing over warm SST accelerates the surface flow more, hence increasing the atmospheric response at the surface and resulting in α_{DMM} growing with U. At high enough U, however, $\tau_{res} \gg \tau_{adv}$, meaning that the lower atmosphere does not fully adjust to the SST forcing feature before being advected beyond it, leading to a weaker coupling. Peak coupling coefficients are hence obtained for $\tau_{res} \approx \tau_{adv}$, and the corresponding surface wind speed is

$$U_{peak} \propto \frac{L_{SST}}{h} \tag{5}$$

In Figure 2a, U_{peak} is smaller for MetOp than for ERA5. According to Equation (5), we argue that this is because SST features in MetOp observations exhibit sharper gradients than in ERA5 [45]. The finer SST features observed by MetOp lead to smaller L_{SST} than those present in reanalysis, and thus resulting in a smaller U_{peak}.

In terms of air stability, measured by $T_{air} - SST$, Figure 2b shows that for both datasets the largest coupling coefficient is obtained for neutral or marginally stable conditions ($T_{air} - SST \in [-1\text{ K}, 3\text{ K}]$). As discussed in Desbiolles et al. (2023) [40], this is related to the fact that the near-surface warming induced by SST features is too weak to destabilise the air column in conditions of strong stability (large positive $T_{air} - SST$) or provide a relevant contribution to the ongoing mixing occurring in unstable conditions (large negative $T_{air} - SST$). The peak in the wind response to underlying SST features is thus obtained for values of $T_{air} - SST$ close to zero.

Despite the overall agreement between the sensitivity of the coupling coefficients on air–sea temperature difference obtained with observational and reanalysis data, a key difference between the two datasets emerges under marginally stable conditions ($T_{air} - SST > 1$ K): while observations indicate a strong coupling, reanalysis displays a large drop in coupling intensity. We interpret the strong coupling in MetOp for marginally stable conditions to be related to the shallow boundary layer that is characteristic of nighttime conditions and upwelling regions: SST structures manifest in large changes in atmospheric properties, given the small air mass present in the boundary layer [8]. Noting that numerical models strongly overestimate the depth of stable boundary layers, as they struggle to correctly represent mixing in the presence of weak and intermittent turbulence and are limited by their vertical resolution [46,64], our interpretation is also consistent

with the smaller coupling coefficients obtained in ERA5 than in MetOp. ERA5 coupling coefficients corresponding to strongly stable and unstable conditions have been rejected due to nonlinearities and not for scarcity of data, as their distribution compared to the MetOp one in Figure 2d suggests.

By considering the combined dependence of the coupling coefficient as a function of U and $T_{air} - SST$ from MetOp data, the first feature that emerges is that there is a much stronger dependence on the air stability than on the background wind speed (Figure 3a), in agreement with the previously published results based on ERA5 data [40]. Moreover, it can be noticed that U_{peak} is about 5 m/s for $T_{air} - SST \simeq 0$ K, and it increases to about 7 m/s for stable conditions ($T_{air} - SST \simeq 2$ K), where the boundary layer is expected to be shallower. This confirms the hypothesis described above on the leading role of h in determining both τ_{res} and the intensity of the atmospheric response to the SST forcing.

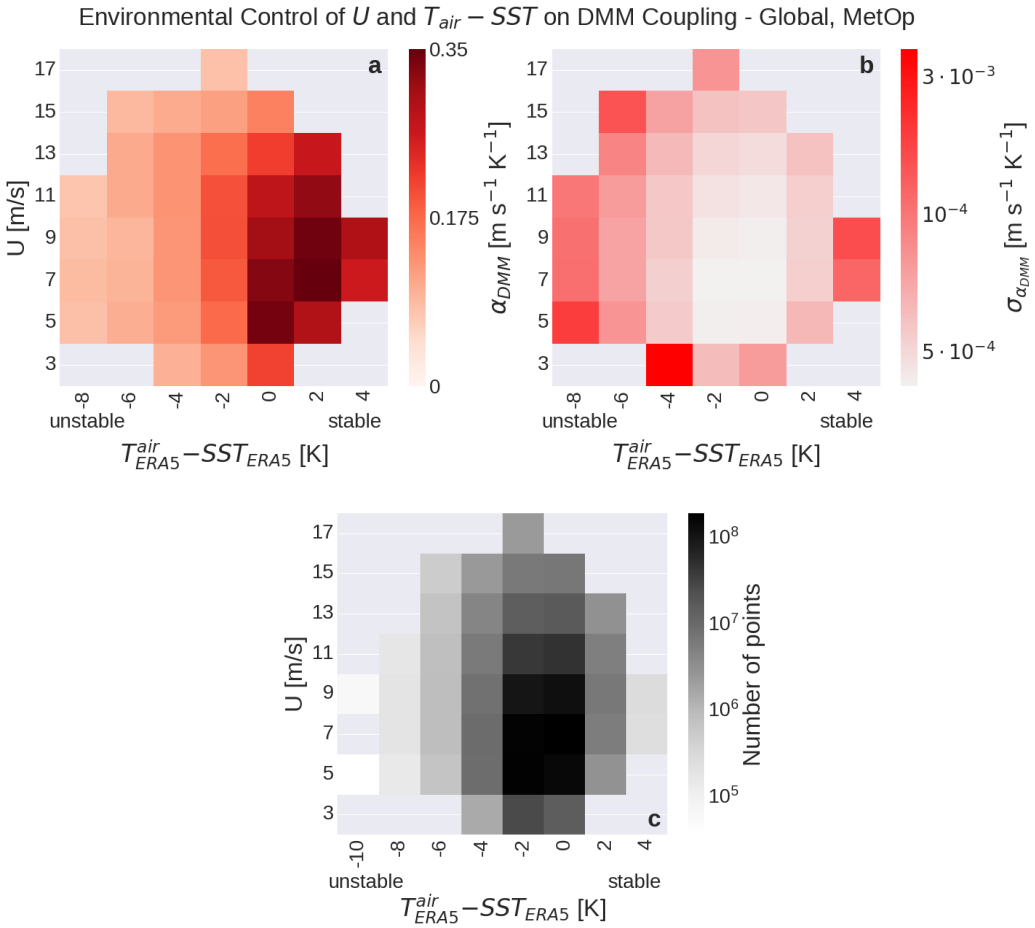

Figure 3. Combined dependence of α_{DMM} on U and $T_{air} - SST$ (**a**) from global MetOp data with the corresponding standard deviation (**b**) and population distribution (**c**).

3.2. Regional Characterisation of Air–Sea Coupling

The regional analyses (Figure 4) support the interpretation, derived from the global analysis, regarding the larger SST length scales in ERA5 and its misrepresentation of coupling under stable conditions. However, certain aspects warrant closer examination.

MetOp data over mid-latitude regions show strong similarity with the global analysis, suggesting that these regions contribute the most to the global behaviour (Figure 4a,b). In fact, they display an increase in coupling strength for increasing wind speed, followed by a peak and a subsequent decrease (Figure 4a). In terms of air stability, they display an increase for marginally unstable conditions, followed by a sort of plateau for stable conditions (Figure 4b).

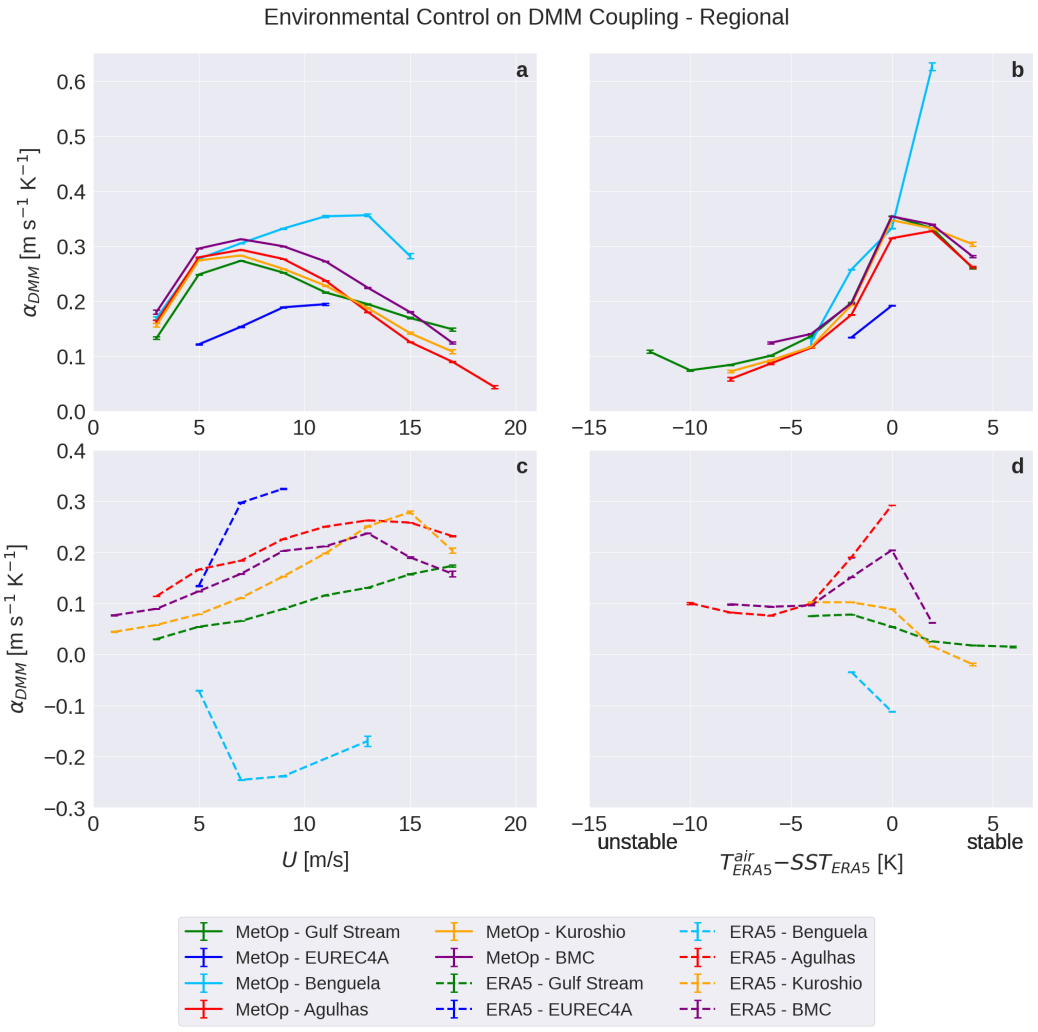

Figure 4. DMM coupling coefficient α_{DMM} as a function of large-scale surface wind speed U (**a**,**c**) and air–sea temperature difference $T_{air} - SST$ (**b**,**d**) from regional observations (**a**,**b**) and reanalysis data (**c**,**d**).

The analysed tropical areas, instead, provide different results. First, the value of U_{peak} is larger than for the mid-latitudes. Then, in the Benguela region the coupling coefficients are larger, with exceptionally high coupling intensity obtained for marginally stable conditions. This is consistent with the fact that the colder waters of the Benguela upwelling system induce a shallow MABL [65], for which the SST forcing induces a strong response due to the smaller amount of air to be affected. The EUREC^{4}A region shows strong nonlinearities in its coupling curves (not shown), hindering the evaluation of the coupling through our linear metrics.

Considering ERA5 data, instead, unlike for MetOp, mid-latitude regions' curves as a function of U exhibit a wider spread and peak at different locations (Figure 4c). The lowest peak is found in the Agulhas Current, with $U_{peak} \approx 13$ m/s, whereas the Gulf Stream shows no decreasing tendency within the available U range. The computation of the coupling coefficient over the tropical region reveals numerous nonlinearities, resulting in the exclusion of a substantial portion of the data. Considering the remaining points, the EUREC^{4}A region exhibits stronger coupling intensity than the observations, which is unexpected given the absence of fine-scale features in ERA5 [66], while the Benguela Current displays negative coupling values, in sharp disagreement with the physical understanding of DMM. Strong nonlinearities also affect the analysis of the $T_{air} - SST$ influence on the coupling intensity, especially over the tropics, the Gulf Stream and the Kuroshio

Current, while the remaining mid-latitude regions show a behaviour compatible with the MetOp data (Figure 4d).

Overall, this investigation indicates that observations lead to a more linear dependence between wind divergence and SST gradient than ERA5 data, and a more consistent dependence of α_{DMM} on the environmental conditions at a regional level. Instead, ERA5 data exhibit pronounced nonlinearities and regional differences, likely stemming from known biases in the ERA5 numerical model related to the representation of the stable boundary layer and lower-tropospheric mixing [36,64,67].

3.3. Dependence of Coupling on SST Structures Spatial Scale

We here verify that for larger length scales of the SST features, the peak coupling happens at larger U, as indicated by Equation (5). To this aim, we low-pass filter MetOp data before computing the coupling coefficients, effectively reducing the SST and wind field resolution and therefore artificially increasing L_{SST} (Figure 5). Two Gaussian filters with standard deviations of 15 km and a 25 km have been used. The coupling coefficients computed on the smoothed data show, respectively, $U_{peak} \approx 9$ m/s and $U_{peak} \approx 11$ m/s, while it was $U_{peak} \approx 7$ m/s for the unfiltered (finer scale) data. This clearly indicates that U_{peak} increases with increasing L_{SST}.

This analysis also supports our interpretation of the larger U_{peak} obtained using ERA5 data, which resolves coarser SST features with respect to MetOp. Similarly, the difference in U_{peak} between mid-latitude and tropical regions in Figure 4 is consistent with the fact that the SST features characteristic length decreases with latitude as the first baroclinic Rossby radius of deformation [68].

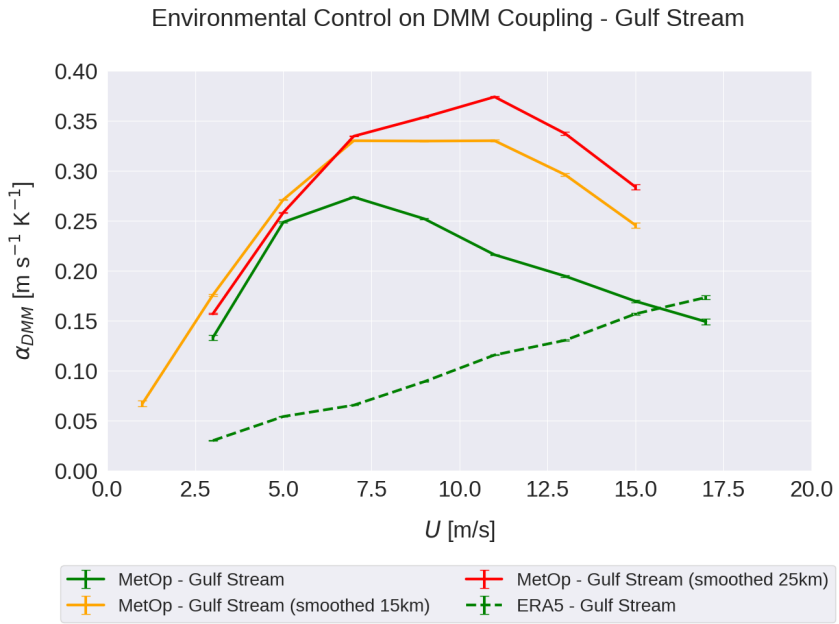

Figure 5. DMM coupling coefficient as a function U over the Gulf Stream. Data corresponding to the original resolution (green, full line) and Gaussian-filter smoothed data (orange with $\sigma = 15$ km, red with $\sigma = 25$ km) are shown. The ERA5 corresponding curve (green, dashed line) is reported for comparison.

3.4. Empirical Model for the Large-Scale Wind Dependence

The fact that the dependence of α_{DMM} on U is non-monotonic for both ERA5 and MetOp data indicates its robustness. In its initial interpretation, brought forward by [40] and summarised above, the dependence on U only appears in the advective time scale

τ_{adv}. Here, by arguing that U also affects the response time scale τ_{res}, we develop a more comprehensive empirical model of α_{DMM} as a function of U.

We hypothesise that DMM generates a surface wind anomaly u'_{DMM} with the following characteristics:

1. u'_{DMM} is a fraction of the large-scale wind U;
2. The ratio τ_{adv}/τ_{res} controls the efficiency of the process as an exponential decay.

Thus, we write

$$u'_{DMM} = \gamma U(1 - e^{-\tau_{adv}/\tau_{res}}), \tag{6}$$

where γ represents the fraction of U that would be observed at the surface due to mixing in the case of an instantaneous atmospheric response ($\tau_{adv} \gg \tau_{res}$, so that $u'_{DMM} \to \gamma U$). Instead, for a very slow response, $\tau_{adv} \ll \tau_{res}$, the mixing is inefficient and no surface DMM wind anomaly is produced, so $u'_{DMM} \to 0$.

The value of γ can be thought as increasing for increasing surface instability, namely,

$$\gamma = \gamma_{neutral} - \Gamma(T_{air} - SST), \tag{7}$$

where $\gamma_{neutral}$ accounts for neutral conditions, $\Gamma > 0$ is a constant, and

$$T_{air} = T_0 - \alpha_T(T_0 - SST) = \tilde{T}_0 + \alpha_T\, SST, \tag{8}$$

with T_0 representing the large-scale air temperature, $\tilde{T}_0 = T_0(1 - \alpha_T)$ independent of the SST, and α_T an adjustment scale of air temperature to the underlying SST. From Equations (7) and (8) follows

$$\begin{gathered} \gamma = \gamma_{neutral} - \Gamma\, \tilde{T}_0 + \Gamma\, (1{-}\alpha_T)\, SST = \gamma_0 + \Gamma'\, SST \\ \gamma_0 = \gamma_{neutral} - \Gamma\, \tilde{T}_0 \quad , \quad \Gamma' = \Gamma\, (1 - \alpha_T). \end{gathered} \tag{9}$$

With these assumptions, the DMM coupling coefficient estimated from the data α_{DMM} can be expressed as

$$\alpha_{DMM} = \frac{\partial u'_r/\partial r}{\partial SST/\partial r} \approx \frac{\delta u'_r}{\delta SST} = \frac{\delta u'_0}{\delta SST} + \frac{\delta u'_{DMM}}{\delta SST} = \alpha_0 + \hat{\alpha}_{DMM}, \tag{10}$$

where u'_0 represents the surface wind speed anomaly generated by other processes than DMM and

$$\hat{\alpha}_{DMM} = \Gamma' U(1 - e^{-\tau_{adv}/\tau_{res}}). \tag{11}$$

From Equations (3) and (4), we obtain

$$\frac{\tau_{adv}}{\tau_{res}} \propto \frac{L_{SST}}{Uh}. \tag{12}$$

Drawing from the extensive literature on the scaling of the MABL height with surface fluxes and, thus, with the wind speed, we can model $h \propto U^{\mu}$ with $\mu \in [0.5, 2]$ according to different models, and as a function of the air stability [63,69,70]. From here,

$$\frac{\tau_{adv}}{\tau_{res}} = \frac{cL_{SST}}{U^{\nu}} \tag{13}$$

with $\nu = \mu + 1 \in [1.5, 3]$ and c being a constant. This leads to

$$\hat{\alpha}_{DMM} = \Gamma U(1 - e^{-cL_{SST}/U^{\nu}}), \quad \nu > 1.5. \tag{14}$$

The simplified model for the coupling coefficient in Equation (14) captures the behaviour observed in the data: α_{DMM} increases linearly with U for small U, it reaches a peak and then decays to zero as $U^{1-\nu}$, assuming $\nu > 1$ from the literature [63]. Moreover, if τ_{res} was independent of the environmental conditions, as proposed by Desbiolles et al. (2023) [40], we would have $\nu = 1$ and there would be no decay for large U. This indicates that it is necessary to include a scaling of h with U to properly model the data.

Since Kitaigorodskii et al. show a different scaling of $h(U)$ depending on stability [70], we treat stable ($T_{air} - SST > 1$ K) and unstable ($T_{air} - SST < -1$ K) conditions separately.

In unstable conditions, a possible scaling of h with U comes from $h \approx \sqrt{|B|}$, where B is the surface buoyancy flux [70], that scales as $B \approx U$ using a bulk formulation approach. Thus, for unstable conditions, $h \approx U^{1/2}$, so that $\mu = 1/2$ and $\nu = 3/2$.

In stable conditions, instead,

$$h \propto L_* \approx \frac{{u_*}^3}{B} \approx \frac{U^3}{U} \approx U^2 \tag{15}$$

with L_* being the Obukhov length [62] and exploiting the scaling of the friction velocity $u_* \approx U$. This leads to $\mu = 2$ and $\nu = 3$.

Despite those scaling predicted values for ν, we keep it as a free parameter in the model and use the data to empirically obtain its value, together with the values of Γ' and cL_{SST}. The description of the fitting procedure is reported in Appendix A.

Assuming that the dynamic regimes and the statistics of L_{SST} are comparable in the mid-latitudes, we aggregate their data to increase the robustness of the results. Tropical regions present almost no data for $U > U_{peak}$ to perform the fit, and therefore their analysis is not shown. The fit reasonably agrees with the observed data both in stable and unstable conditions (Figure 6). In particular, in both cases, the decay for large U is guaranteed by $\nu > 1$. From the fit of the aggregated mid-latitude data we obtain $\nu_{mid\ lats} = 2.1$ in unstable conditions, slightly overestimating the reference value $\nu_{ref} = 3/2$, and $\nu_{mid\ lats} = 2.5$ in stable conditions, slightly underestimating the reference value $\nu_{ref} = 3$, but coherent with other h scalings in the literature [63,69,71].

Our physical understanding suggests that the first baroclinic Rossby radius of deformation can represent the characteristic length scale of the SST forcing features. We can exploit the empirical model introduced above to argue that the data agree with this. In fact, we can compute the analytical peak velocity U_{peak} by setting the first derivative of $\hat{\alpha}_{DMM}$ equal to zero, namely,

$$\frac{\partial \hat{\alpha}_{DMM}}{\partial U} = 0, \tag{16}$$

which gives an implicit definition of U_{peak} as a function of L_{SST} as

$$1 + \nu \frac{cL_{SST}}{U_{peak}^{\nu}} = e^{cL_{SST}/U_{peak}^{\nu}}. \tag{17}$$

As ν is dependent on the stability conditions, we computed the regional trends of α_{DMM}, as in Figure 4, now separating stable and unstable conditions. Employing our estimate of $\nu = 2.1$ from the fit for unstable conditions, we can estimate the peak velocities as the maximum of the curve of the MetOp data in the Gulf Stream and the Benguela regions, which correspond to 7 m/s and 12 m/s, respectively. Then, with the implicit function, we estimate the corresponding values of cL_{SST} and compute their ratio, as the constant c contains many free parameters that we are not able to constrain at this stage (Figure 7). Supposing, then, that c is the same in both regions, the ratio $L_{SST}^{Gulf\ Stream}/L_{sst}^{Benguela} \approx 0.39$ can be computed and it is verified to be in agreement with the ratio of the first baroclinic Rossby radius of deformation for the two regions [68].

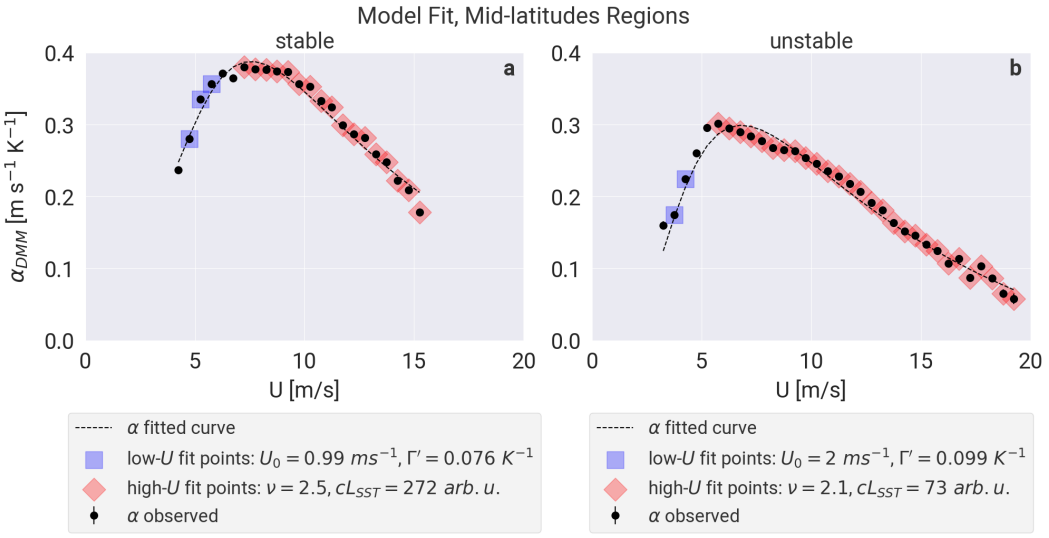

Figure 6. Coupling coefficients as a function of U for all mid-latitude regions in stable (**a**) and unstable (**b**) conditions. Blue points denote the data used to perform the linear fit in Equation (A1) for low-U. Red points are employed to fit the function for high U in Equation (A2), estimating ν and cL_{SST}. Dashed lines show the final curves of the fit, with the relevant parameters indicated in the legend.

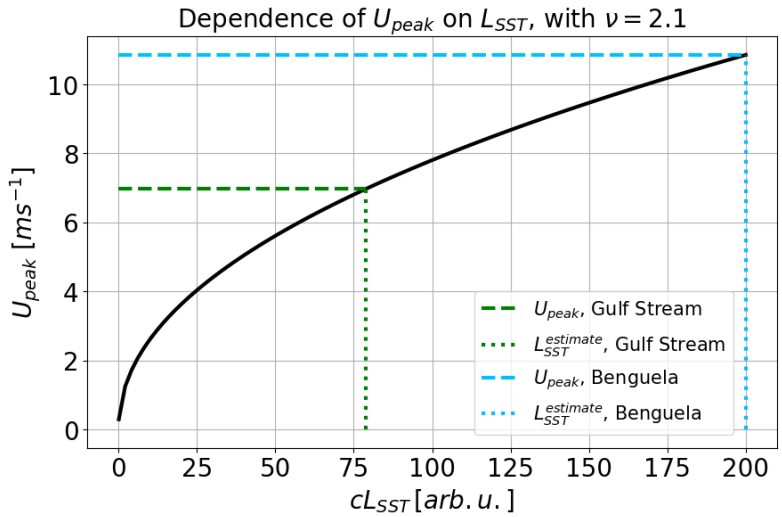

Figure 7. Dependence of the peak wind speed U_{peak} as a function of the SST characteristic length scale L_{SST} multiplied by the factor c, obtained from Equation (17) for $\nu = 2.1$ (black solid line). Horizontal dashed lines represent the observed U_{peak} values for the Gulf Stream (green) and the Benguela Current (light blue), and vertical dotted ones the corresponding L_{SST} values.

4. Discussion

The coupling coefficients computed on observational satellite data and on ERA5 reanalysis have different dependencies on environmental conditions. Part of the discrepancies might be due to the different methodologies applied on the two products, that are now discussed to assess the sensitivity of the results. We investigated the influence of the different standard deviation of the Gaussian filter (σ) used to separate large-scale wind from surface wind anomalies in observations ($\sigma = 50$ km, following Meroni et al. (2023) [37]) and reanalysis ($\sigma = 450$ km, following Desbiolles et al. (2023) [40]). Very little variability in the coupling coefficient behaviour was observed when testing for different σ in both products. In fact, the coupling coefficients are expected to change significantly for scales larger than 500 km [2,33], which were removed in all the tests performed. Moreover, spatial derivatives applied to wind-field anomalies in the coupling coefficient computation act as a high-pass

filter, reducing the sensitivity of the analysis to the Gaussian filter size. For these reasons, although the filters used in the two analyses differ by roughly one order of magnitude, both coupling coefficient estimates are representative of mesoscale dynamics, and therefore their behaviour with respect to the environmental conditions is comparable.

Differently from ERA5, L3C SST observations are available only in clear-sky conditions, as the AVHRR instrument is not able to observe the sea surface through clouds. As an alternative, ESA-CCI L4 SST products do not present this limitation, as they consist of daily gap-filled fields. However, employing the L4 SST product here would entail losing the instantaneous colocation with MetOp ASCAT L2 wind observations, which we aim to preserve. On the other hand, tests performed over the Gulf Stream indicate that only 95% of the ERA5 data have cloud cover larger than 20%, and clear-sky conditions are mostly found near the coast, introducing an unintended geographical bias. For those reasons, we cannot rule out the possibility that cloudiness has different implications in the two datasets.

As mentioned in Section 2, MetOp instantaneous observations consist of equivalent neutral wind and skin SST, while we use 10 m wind and foundation SST from ERA5. In general, the use of the equivalent neutral wind instead of the 10 m wind might result in a slightly different value of wind divergence. Only in the case of a change in sign of the air–sea temperature difference while crossing an SST front might this result in an important change in wind divergence, which would artificially increase the coupling coefficient [72]. Thus, we expect this difference to be relevant only in the case of large-scale neutral conditions (i.e., in the vicinity of $T_{air} - SST \approx 0$) and not to affect the overall dependence of the scaling of α_{DMM} as a function of the environmental variables considered. In terms of SST, instead, the use of a satellite-based foundation SST product (such as the L4 ESA-CCI dataset) typically comes with an inherent smoothing due to the corrections introduced to derive it [50]. This has been shown to reduce the DMM coupling coefficients in the study areas, because of the smoother scales and the time mismatch between the wind and SST data [37]. As this is expected to introduce a constant bias, we do not think that it can influence our results.

Regional analyses show a widespread variability in the coupling behaviour which is not captured by the characterisation of the atmospheric conditions through U and $T_{air} - SST$ solely. The nature and localisation of these discrepancies suggest the relevance of h and L_{SST}, but some of the assumptions and hypotheses formulated in this work deserve a more thorough investigation, that we aim to address in a future dedicated study. The use of L_{SST} as a proxy of the SST gradients length scale yields the correct scaling, as shown in Figure 7, but looking into the spectral features of a high-resolution gap-filled SST field would provide a more solid confirmation of our interpretation. The unexpected results observed for stable regimes suggest that a characterisation of the MABL vertical profiles, together with a more complete description of τ_{res} including the momentum eddy diffusion coefficient, could provide additional insights to explain uncaptured behaviours. Moreover, our estimates of ν are compatible with the ones in the literature within the assumption that $\tau_{res} \propto h$, as presented in Section 3.4. However, other formulations of τ_{res} can be found in the literature, e.g., Small et al. (2008) [3] suggest $\tau_{res} \propto h^2$, such that $\nu^{unstable} = 2$ and, more notably, $\nu^{stable} = 5$, a value twice as large as our estimate. We believe high-resolution coupled numerical simulations to be the most suitable tool to address these open issues, and we aim to exploit their potential in future work aiming to further advance the understanding of this topic.

5. Conclusions

Mesoscale air–sea interactions have an important impact on surface fluxes, cloudiness, rainfall, and MABL dynamics, with potential inverse-cascade effects at larger

scales [3,7,9–13,15,16]. Previous works have highlighted the dependency of air–sea coupling on environmental conditions such as surface wind, atmospheric stability and Rossby number at the regional level using satellite data [41,48], in-situ observations [8], and numerical simulations [39]. In particular, Desbiolles et al. (2023) [40] found a relevant role of large-scale surface wind (U) and air–sea temperature difference ($T_{air} - SST$) in modulating the coupling intensity between sea surface temperature (SST) and surface wind using global ERA5 reanalysis data. Studies comparing numerical simulations indicate that the model representation of these air–sea interactions is influenced by the design of atmosphere-ocean coupling, the spatial and temporal resolutions, and the choice of the MABL scheme [25,32,33], underscoring the need for analysis on observational data to properly understand the physical processes.

In this work, we analyse the dependence of the DMM coupling on U and $T_{air} - SST$ using MetOp A satellite data of ASCAT surface wind and AVHRR SST. Although observations confirm the overall physical interpretation of the control of U and $T_{air} - SST$ on the mesoscale SST-wind coupling emerging from global ERA5 data, we highlight relevant differences compared to reanalysis data [40]. Due to its coarser resolution, ERA5 presents a larger SST characteristic length scale (L_{SST}) than the satellite observations. This corresponds to larger advective timescales, which determines the shape of the coupling coefficient as a function of U, with the peak occurring at a larger velocity. With respect to $T_{air} - SST$, ERA5 does not properly represent the coupling in the stable regime for reasons possibly linked to the difficulties in the numerical representation of turbulence in these conditions [64]. Moreover, widespread nonlinearities revealed in regional analyses indicate that ERA5 may lack the ability to adequately represent these interactions in specific atmospheric conditions and regional contexts. These findings highlight the need for high-resolution observational studies to investigate mesoscale and submesoscale air–sea interactions and to support and advance these interpretations.

The absence of high-resolution satellite measurements of MABL properties such as stability, surface fluxes, and cloudiness constitutes a critical limitation that can also partially be addressed with high-resolution numerical simulations. Nevertheless, recent studies have demonstrated important progress from the remote-sensing observational point of view: surface fluxes have been inferred from SAR (Synthetic Aperture Radar) roughness data, enabling estimates of atmospheric stability at resolutions of O(10 km) [73], and SAR observations are being employed to retrieve surface winds at scales of O(1 km), albeit with certain limitations [74,75]. To overcome this gap, the European Space Agency (ESA) will launch the Earth Explorer 10 mission Harmony in 2029, designed to provide SAR imagery obtained from a novel dual line-of-sight geometry together with O(1 km) SST observations. This mission will provide the necessary observation to perform a systematic assessment of air–sea interactions at the meso- and submesoscale based on instantaneous observations, with the potential to advance the understanding of their link with low-level clouds, thereby significantly improving the representation of the Earth's radiative balance.

Supplementary Materials: The following supporting information can be downloaded at https://www.mdpi.com/article/10.3390/rs17223764/s1, Table S1: Geographical Regions; Figure S1: Sensitivity test of rejection conditions in the linear regression computation of α_{DMM}. Reference [48] is cited in the supplementary materials.

Author Contributions: Conceptualization, L.F.D., A.N.M. and C.P.; methodology, L.F.D., A.N.M. and C.P.; software, L.F.D.; validation, L.F.D.; formal analysis, L.F.D.; investigation, L.F.D.; resources, C.P.; data curation, L.F.D.; writing—original draft preparation, L.F.D.; writing—review and editing, L.F.D., A.N.M. and C.P.; visualization, L.F.D.; supervision, C.P. and A.N.M.; project administration, C.P.; funding acquisition, C.P. All authors have read and agreed to the published version of the manuscript.

Funding: This work is an outcome of the Project "Science Data Utilisation and Impact Study for Ocean—HRMNY DUIST" (ESA contract no. 4000135827/21/NL/FF/an).

Data Availability Statement: SST data from MetOp A AVHRR instrument (https://cds.climate.copernicus.eu/datasets/satellite-sea-surface-temperature?tab=overview, accessed on 14 November 2025) and ERA5 reanalysis data (hourly: https://cds.climate.copernicus.eu/datasets/reanalysis-era5-single-levels?tab=overview, accessed on 14 November 2025; daily: https://cds.climate.copernicus.eu/datasets/derived-era5-single-levels-daily-statistics?tab=overview, accessed on 14 November 2025) have been downloaded from Copernicus Climate Change Service (C3S) Climate Data Store (CDS) portal. Surface wind data from MetOp A ASCAT instrument (https://search.earthdata.nasa.gov/search/granules/collection-details?p=C1996881752-POCLOUD&pg[0][v]=f&tl=1459528650.5!5!!, accessed on 14 November 2025) come from NASA EarthDATA portal. Scripts for pre-processing and analysis are available on GitHub (https://github.com/lfdavoli/ASI_RS_MDPI.git, accessed on 14 November 2025).

Acknowledgments: This work has been conducted in collaboration with the Italian Research Ministry Project "Dipartimenti di Eccellenza 2023–2027". We would like to thank Alessandro Storer, Matteo Borgnino, Fabien Desbiolles, Lionel Renault, Paco Lopez Dekker, Louise Nuijens, Owen O'Driscoll, Jacotte Monroe, Edoardo Foschi, Pouriya Alinaghi, and Geet George for the valuable discussions that contributed to this work.

Conflicts of Interest: The authors declare no conflicts of interest. The funders had no role in the design of the study; in the collection, analyses, or interpretation of data; in the writing of the manuscript; or in the decision to publish the results.

Appendix A. Empirical Model Fitting

We adopt a 2-step fitting procedure for the empirical model parameter estimation, whose results are plotted in Figure 6. First, we expect α_{DMM} to scale with U for $U_0 < U < U_{peak}$, so we fit coupling coefficient estimates in this interval (Figure 6, in blue) with a function in the form

$$\alpha = \alpha_0 + \Gamma' U \tag{A1}$$

obtaining the estimates of α_0, Γ' and $U_0 = -\alpha_0/\Gamma'$ reported in the legend. From a physical point of view, α_0 is the contribution of fine-scale phenomena other than DMM, such that $\alpha_0 \gg \hat{\alpha}_{DMM}$ for $U < U_0$, and $\alpha_0 \ll \hat{\alpha}_{DMM}$ for $U > U_0$, U_0 being the threshold wind speed at which DMM becomes the dominant mesoscale process in the along-U direction.

Then, we employ Γ' and α_0 from the previous step and fit points in $U \geq U_{peak}$ (Figure 6, in red), where we expect the decrease led by the parentheses in Equation (14) to be controlled by ν and cL_{SST}. We estimate their values from, respectively, the slope and the intercept of the linear fit

$$\log\left[-\log\left(1-\frac{\alpha-\alpha_0}{\Gamma' U}\right)\right] = \log(cL_{SST}) - \nu\ \log(U) \tag{A2}$$

obtained from Equations (10) and (14).

References

1. Liu, W.T.; Zhang, A.; Bishop, J.K. Evaporation and solar irradiance as regulators of sea surface temperature in annual and interannual changes. *J. Geophys. Res. Ocean.* **1994**, *99*, 12623–12637. [CrossRef]
2. Chelton, D.B.; Xie, S.P. Coupled ocean-atmosphere interaction at oceanic mesoscales. *Oceanography* **2010**, *23*, 54–69. [CrossRef]
3. Small, R.J.; deSzoeke, S.P.; Xie, S.P.; O'Neill, L.; Seo, H.; Song, Q.; Cornillon, P.; Spall, M.; Minobe, S. Air–sea interaction over ocean fronts and eddies. *Dyn. Atmos. Ocean.* **2008**, *45*, 274–319. [CrossRef]
4. Seo, H.; O'Neill, L.W.; Bourassa, M.A.; Czaja, A.; Drushka, K.; Edson, J.B.; Fox-Kemper, B.; Frenger, I.; Gille, S.T.; Kirtman, B.P.; et al. Ocean Mesoscale and Frontal-Scale Ocean-Atmosphere Interactions and Influence on Large-Scale Climate: A Review. *J. Clim.* **2023**, *36*, 1981–2013. [CrossRef]

5. Rai, S.; Hecht, M.; Maltrud, M.; Aluie, H. Scale of oceanic eddy killing by wind from global satellite observations. *Sci. Adv.* **2021**, *7*, eabf4920. [CrossRef]
6. Gentemann, C.L.; Clayson, C.A.; Brown, S.; Lee, T.; Parfitt, R.; Farrar, J.T.; Bourassa, M.; Minnett, P.J.; Seo, H.; Gille, S.T.; et al. FluxSat: Measuring the Ocean–Atmosphere Turbulent Exchange of Heat and Moisture from Space. *Remote Sens.* **2020**, *12*, 1796. [CrossRef]
7. Chelton, D.B.; Schlax, M.G.; Freilich, M.H.; Milliff, R.F. Satellite Measurements Reveal Persistent Small-Scale Features in Ocean Winds. *Science* **2004**, *303*, 978–983. [CrossRef]
8. Acevedo, O.C.; Pezzi, L.P.; Souza, R.B.; Anabor, V.; Degrazia, G.A. Atmospheric boundary layer adjustment to the synoptic cycle at the Brazil-Malvinas Confluence, South Atlantic Ocean. *J. Geophys. Res. Atmos.* **2010**, *115*, D22107. [CrossRef]
9. Minobe, S.; Kuwano-Yoshida, A.; Komori, N.; Xie, S.P.; Small, R.J. Influence of the Gulf Stream on the troposphere. *Nature* **2008**, *452*, 206–209. [CrossRef] [PubMed]
10. Minobe, S.; Miyashita, M.; Kuwano-Yoshida, A.; Tokinaga, H.; Xie, S.P. Atmospheric response to the Gulf Stream: Seasonal variations. *J. Clim.* **2010**, *23*, 3699–3719. [CrossRef]
11. Small, R.J.; Rousseau, V.; Parfitt, R.; Laurindo, L.; O'Neill, L.; Masunaga, R.; Schneider, N.; Chang, P. Near-Surface Wind Convergence over the Gulf Stream—The Role of SST Revisited. *J. Clim.* **2023**, *36*, 5527–5548. [CrossRef]
12. Ma, X.; Jing, Z.; Chang, P.; Liu, X.; Montuoro, R.; Small, R.J.; Bryan, F.O.; Greatbatch, R.J.; Brandt, P.; Wu, D.; et al. Western boundary currents regulated by interaction between ocean eddies and the atmosphere. *Nature* **2016**, *535*, 533–537. [CrossRef]
13. Frenger, I.; Gruber, N.; Knutti, R.; Münnich, M. Imprint of Southern Ocean eddies on winds, clouds and rainfall. *Nat. Geosci.* **2013**, *6*, 608–612. [CrossRef]
14. Pezzi, L.P.; de Souza, R.B.; Santini, M.F.; Miller, A.J.; Carvalho, J.T.; Parise, C.K.; Quadro, M.F.; Rosa, E.B.; Justino, F.; Sutil, U.A.; et al. Oceanic eddy-induced modifications to air–sea heat and CO_2 fluxes in the Brazil-Malvinas Confluence. *Sci. Rep.* **2021**, *11*, 10648. [CrossRef]
15. Parfitt, R.; Czaja, A.; Minobe, S.; Kuwano-Yoshida, A. The atmospheric frontal response to SST perturbations in the Gulf Stream region. *Geophys. Res. Lett.* **2016**, *43*, 2299–2306. [CrossRef]
16. Hirata, H.; Kawamura, R.; Nonaka, M.; Tsuboki, K. Significant Impact of Heat Supply From the Gulf Stream on a "Superbomb" Cyclone in January 2018. *Geophys. Res. Lett.* **2019**, *46*, 7718–7725. [CrossRef]
17. Gaube, P.; Chickadel, C.C.; Branch, R.; Jessup, A. Satellite Observations of SST-Induced Wind Speed Perturbation at the Oceanic Submesoscale. *Geophys. Res. Lett.* **2019**, *46*, 2690–2695. [CrossRef]
18. Strobach, E.; Klein, P.; Molod, A.; Fahad, A.A.; Trayanov, A.; Menemenlis, D.; Torres, H. Local Air-Sea Interactions at Ocean Mesoscale and Submesoscale in a Western Boundary Current. *Geophys. Res. Lett.* **2022**, *49*, e2021GL097003. [CrossRef]
19. Renault, L.; Contreras, M.; Marchesiello, P.; Conejero, C.; Uchoa, I.; Wenegrat, J. Unraveling the Impacts of Submesoscale Thermal and Current Feedbacks on the Low-Level Winds and Oceanic Submesoscale Currents. *J. Phys. Oceanogr.* **2024**, *54*, 2463–2486. [CrossRef]
20. Bai, Y.; Thompson, A.F.; Bôas, A.B.V.; Klein, P.; Torres, H.S.; Menemenlis, D. Sub-Mesoscale Wind-Front Interactions: The Combined Impact of Thermal and Current Feedback. *Geophys. Res. Lett.* **2023**, *50*, e2023GL104807. [CrossRef]
21. Conejero, C.; Renault, L.; Desbiolles, F.; McWilliams, J.C.; Giordani, H. Near-Surface Atmospheric Response to Meso- and Submesoscale Current and Thermal Feedbacks. *J. Phys. Oceanogr.* **2024**, *54*, 823–848. [CrossRef]
22. Nuijens, L.; Wenegrat, J.; Dekker, P.L.; Pasquero, C.; O'Neill, L.W.; Ardhuin, F.; Ayet, A.; Bechtold, P.; Bruch, W.; Laurindo, L.; et al. The air-sea interaction (ASI) submesoscale: Physics and impact. In Proceedings of the Lorentz-Center Workshop, Leiden, The Netherlands, 25–29 September 2023. [CrossRef]
23. Renault, L.; Molemaker, M.J.; Mcwilliams, J.C.; Shchepetkin, A.F.; Lemarié, F.; Chelton, D.; Illig, S.; Hall, A. Modulation of Wind Work by Oceanic Current Interaction with the Atmosphere. *J. Phys. Oceanogr.* **2016**, *46*, 1685–1704. [CrossRef]
24. Takatama, K.; Schneider, N. The Role of Back Pressure in the Atmospheric Response to Surface Stress Induced by the Kuroshio. *J. Atmos. Sci.* **2017**, *74*, 597–615. [CrossRef]
25. Renault, L.; Masson, S.; Oerder, V.; Jullien, S.; Colas, F. Disentangling the Mesoscale Ocean-Atmosphere Interactions. *J. Geophys. Res. Ocean.* **2019**, *124*, 2164–2178. [CrossRef]
26. Wallace, J.M.; Mitchell, T.P.; Deser, C. The Influence of Sea-Surface Temperature on Surface Wind in the Eastern Equatorial Pacific: Seasonal and Interannual Variability. *J. Clim.* **1989**, *2*, 1492–1499. [CrossRef]
27. Hayes, S.P.; McPhaden, M.J.; Wallace, J.M. The Influence of Sea-Surface Temperature on Surface Wind in the Eastern Equatorial Pacific: Weekly to Monthly Variability. *J. Clim.* **1989**, *2*, 1500–1506. [CrossRef]
28. Lindzen, R.S.; Nigam, S. On the Role of Sea Surface Temperature Gradients in Forcing Low-Level Winds and Convergence in the Tropics. *J. Atmos. Sci.* **1987**, *44*, 2418–2436. [CrossRef]
29. Desbiolles, F.; Alberti, M.; Hamouda, M.E.; Meroni, A.N.; Pasquero, C. Links Between Sea Surface Temperature Structures, Clouds and Rainfall: Study Case of the Mediterranean Sea. *Geophys. Res. Lett.* **2021**, *48*, e2020GL091839. [CrossRef]

30. Chelton, D.B.; Esbensen, S.K.; Schlax, M.G.; Thum, N.; Freilich, M.H.; Wentz, F.J.; Gentemann, C.L.; Mcphaden, M.J.; Schopf, P.S. Observations of Coupling between Surface Wind Stress and Sea Surface Temperature in the Eastern Tropical Pacific. *J. Clim.* **2001**, *14*, 1479–1498. [CrossRef]
31. O'Neill, L.W.; Chelton, D.B.; Esbensen, S.K. Observations of SST-Induced Perturbations of the Wind Stress Field over the Southern Ocean on Seasonal Timescales. *J. Clim.* **2003**, *16*, 2340–2354. [CrossRef]
32. Bryan, F.O.; Tomas, R.; Dennis, J.M.; Chelton, D.B.; Loeb, N.G.; Mcclean, J.L. Frontal Scale Air–Sea Interaction in High-Resolution Coupled Climate Models. *J. Clim.* **2010**, *23*, 6277–6291. [CrossRef]
33. Mishra, A.K.; Meroni, A.N.; Strobach, E.; Jangir, B. Effects of the Grid Spacing and Background Wind on the Daily Air-Sea Coupling Over the Mediterranean Sea in HighResMIP. *J. Geophys. Res. Atmos.* **2025**, *130*, e2024JD041686. [CrossRef]
34. Oerder, V.; Colas, F.; Echevin, V.; Masson, S.; Hourdin, C.; Jullien, S.; Madec, G.; Lemarié, F. Mesoscale SST–wind stress coupling in the Peru–Chile current system: Which mechanisms drive its seasonal variability? *Clim. Dyn.* **2016**, *47*, 2309–2330. [CrossRef]
35. Perlin, N.; Szoeke, S.P.D.; Chelton, D.B.; Samelson, R.M.; Skyllingstad, E.D.; O'neill, L.W. Modeling the Atmospheric Boundary Layer Wind Response to Mesoscale Sea Surface Temperature Perturbations. *Mon. Weather Rev.* **2014**, *142*, 4284–4307. [CrossRef]
36. Sandu, I.; Bechtold, P.; Nuijens, L.; Beljaars, A.; Brown, A. *On the Causes of Systematic Forecast Biases in Near-Surface Wind Direction over the Oceans Near-Surface Wind Direction Biases*; European Centre for Medium Range Weather Forecasts: Reading, UK, 2020. [CrossRef]
37. Meroni, A.N.; Desbiolles, F.; Pasquero, C. Satellite signature of the instantaneous wind response to mesoscale oceanic thermal structures. *Q. J. R. Meteorol. Soc.* **2023**, *149*, 3373–3382. [CrossRef]
38. Meroni, A.N.; Giurato, M.; Ragone, F.; Pasquero, C. Observational evidence of the preferential occurrence of wind convergence over sea surface temperature fronts in the Mediterranean. *Q. J. R. Meteorol. Soc.* **2020**, *146*, 1443–1458. [CrossRef]
39. Foussard, A.; Lapeyre, G.; Plougonven, R. Response of Surface Wind Divergence to Mesoscale SST Anomalies under Different Wind Conditions. *J. Atmos. Sci.* **2019**, *76*, 2065–2082. [CrossRef]
40. Desbiolles, F.; Meroni, A.N.; Renault, L.; Pasquero, C. Environmental Control of Wind Response to Sea Surface Temperature Patterns in Reanalysis Dataset. *J. Clim.* **2023**, *36*, 3881–3893. [CrossRef]
41. Schneider, N. Scale and rossby number dependence of observed wind responses to ocean-mesoscale sea surface temperatures. *J. Atmos. Sci.* **2020**, *77*, 3171–3192. [CrossRef]
42. Rivas, M.B.; Stoffelen, A. Characterizing ERA-Interim and ERA5 surface wind biases using ASCAT. *Ocean Sci.* **2019**, *15*, 831–852. [CrossRef]
43. Vogelzang, J.; Stoffelen, A.; Verhoef, A.; Figa-Saldaña, J. On the quality of high-resolution scatterometer winds. *J. Geophys. Res. Ocean.* **2011**, *116*, C10033. [CrossRef]
44. Bolgiani, P.; Calvo-Sancho, C.; Díaz-Fernández, J.; Quitián-Hernández, L.; Sastre, M.; Santos-Muñoz, D.; Farrán, J.I.; González-Alemán, J.J.; Valero, F.; Martín, M.L. Wind kinetic energy climatology and effective resolution for the ERA5 reanalysis. *Clim. Dyn.* **2022**, *59*, 737–752. [CrossRef]
45. Seethala, C.; Zuidema, P.; Edson, J.; Brunke, M.; Chen, G.; Li, X.Y.; Painemal, D.; Robinson, C.; Shingler, T.; Shook, M.; et al. On Assessing ERA5 and MERRA2 Representations of Cold-Air Outbreaks Across the Gulf Stream. *Geophys. Res. Lett.* **2021**, *48*, e2021GL094364. [CrossRef]
46. Hersbach, H.; Bell, B.; Berrisford, P.; Hirahara, S.; Horányi, A.; Muñoz-Sabater, J.; Nicolas, J.; Peubey, C.; Radu, R.; Schepers, D.; et al. The ERA5 global reanalysis. *Q. J. R. Meteorol. Soc.* **2020**, *146*, 1999–2049. [CrossRef]
47. Bishop, S.P.; Small, R.J.; Bryan, F.O. The Global Sink of Available Potential Energy by Mesoscale Air-Sea Interaction. *J. Adv. Model. Earth Syst.* **2020**, *12*, e2020MS002118. [CrossRef]
48. O'Neill, L.W.; Chelton, D.B.; Esbensen, S.K. Covariability of Surface Wind and Stress Responses to Sea Surface Temperature Fronts. *J. Clim.* **2012**, *25*, 5916–5942. [CrossRef]
49. Embury, O.; Bulgin, C.E.; Mittaz, J. ESA Sea Surface Temperature Climate Change Initiative (SST_cci): Advanced Very High Resolution Radiometer (AVHRR) Level 3 Collated (L3C) Climate Data Record, Version 2.1. 2019. Available online: https://catalogue.ceda.ac.uk/uuid/7db4459605da4665b6ab9a7102fb4875/ (accessed on 14 November 2025).
50. Merchant, C.J.; Embury, O.; Bulgin, C.E.; Block, T.; Corlett, G.K.; Fiedler, E.; Good, S.A.; Mittaz, J.; Rayner, N.A.; Berry, D.; et al. Satellite-based time-series of sea-surface temperature since 1981 for climate applications. *Sci. Data* **2019**, *6*, 223. [CrossRef]
51. Verhoef, A.; Vogelzang, J.; Verspeek, J.; Stoffelen, A. Long-Term Scatterometer Wind Climate Data Records. *IEEE J. Sel. Top. Appl. Earth Obs. Remote Sens.* **2017**, *10*, 2186–2194. [CrossRef]
52. Kettle, A.J. A Diagram of Wind Speed Versus Air-sea Temperature Difference to Understand the Marine atmospheric Boundary Layer. *Energy Procedia* **2015**, *76*, 138–147. [CrossRef]
53. Rayner, N.A.; Parker, D.E.; Horton, E.B.; Folland, C.K.; Alexander, L.V.; Rowell, D.P.; Kent, E.C.; Kaplan, A. Global analyses of sea surface temperature, sea ice, and night marine air temperature since the late nineteenth century. *J. Geophys. Res.* **2003**, *108*, 4407. [CrossRef]

54. Donlon, C.J.; Martin, M.; Stark, J.; Roberts-Jones, J.; Fiedler, E.; Wimmer, W. The Operational Sea Surface Temperature and Sea Ice Analysis (OSTIA) system. *Remote Sens. Environ.* **2012**, *116*, 140–158. [CrossRef]
55. Meroni, A.N.; Desbiolles, F.; Pasquero, C. Introducing New Metrics for the Atmospheric Pressure Adjustment to Thermal Structures at the Ocean Surface. *J. Geophys. Res. Atmos.* **2022**, *127*, e2021JD035968. [CrossRef]
56. Press, W.H.; Teukolsky, S.A.; Vetterling, W.T.; Flannery, B.P. *Numerical Recipes: The Art of Scientific Computing*; Cambridge University Press: Cambridge, UK, 2007; p. 1235.
57. Liu, W.T.; Xie, X. Ocean-atmosphere momentum coupling in the Kuroshio extension observed from space. *J. Oceanogr.* **2008**, *64*, 631–637. [CrossRef]
58. Pezzi, L.P.; Souza, R.B.; Dourado, M.S.; Garcia, C.A.; Mata, M.M.; Silva-Dias, M.A. Ocean-atmosphere in situ observations at the Brazil-Malvinas Confluence region. *Geophys. Res. Lett.* **2005**, *32*, L22603. [CrossRef]
59. O'Neill, L.W.; Chelton, D.B.; Esbensen, S.K.; Wentz, F.J. High-Resolution Satellite Measurements of the Atmospheric Boundary Layer Response to SST Variations along the Agulhas Return Current. *J. Clim.* **2005**, *18*, 2706–2723. [CrossRef]
60. Bane, J.M.; Osgood, K.E. Wintertime air-sea interaction processes across the Gulf Stream. *J. Geophys. Res. Ocean.* **1989**, *94*, 10755–10772. [CrossRef]
61. Stevens, B.; Bony, S.; Farrell, D.; Ament, F.; Blyth, A.; Fairall, C.; Karstensen, J.; Quinn, P.; Speich, S.; Acquistapace, C.; et al. EUREC^{4}A. *Earth Syst. Sci. Data* **2021**, *13*, 4067–4119. [CrossRef]
62. Obukhov, A.M. Turbulence in an atmosphere with a non-uniform temperature. *Bound.-Layer Meteorol.* **1971**, *2*, 7–29. [CrossRef]
63. Zilitinkevich, S.; Baklanov, A. Calculation of the height of the stable boundary layer in practical applications. *Bound.-Layer Meteorol.* **2002**, *105*, 389–409. [CrossRef]
64. Davy, R.; Esau, I. Global climate models' bias in surface temperature trends and variability. *Environ. Res. Lett.* **2014**, *9*, 114024. [CrossRef]
65. Kalmus, P.; Ao, C.O.; Wang, K.N.; Manzi, M.P.; Teixeira, J. A high-resolution planetary boundary layer height seasonal climatology from GNSS radio occultations. *Remote Sens. Environ.* **2022**, *276*, 113037. [CrossRef]
66. Fernández, P.; Speich, S.; Borgnino, M.; Meroni, A.N.; Desbiolles, F.; Pasquero, C. On the importance of the atmospheric coupling to the small-scale ocean in the modulation of latent heat flux. *Front. Mar. Sci.* **2023**, *10*, 1136558. [CrossRef]
67. Sandu, I.; Beljaars, A.; Bechtold, P.; Mauritsen, T.; Balsamo, G. Why is it so difficult to represent stably stratified conditions in numerical weather prediction (NWP) models? *J. Adv. Model. Earth Syst.* **2013**, *5*, 117–133. [CrossRef]
68. Chelton, D.B.; Deszoeke, R.A.; Schlax, M.G.; Naggar, K.E.; Siwertz, N. Geographical Variability of the First Baroclinic Rossby Radius of Deformation. *J. Phys. Oceanogr.* **1998**, *28*, 433–460. [CrossRef]
69. Arya, S.P. Parameterizing the Height of the Stable Atmospheric Boundary Layer. *J. Appl. Meteorol. Climatol.* **1981**, *20*, 1192–1202. [CrossRef]
70. Kitaigorodskii, S.A.; Joffre, S.M. In search of a simple scaling for the height of the stratified atmospheric boundary layer. *Tellus Ser. A* **1988**, *40*, 419–433. [CrossRef]
71. Nieuwstadt, F.T.M. The Turbulent Structure of the Stable, Nocturnal Boundary Layer. *J. Atmos. Sci.* **1984**, *41*, 2202–2216. [CrossRef]
72. Liu, W.T.; Tang, W. *Equivalent Neutral Wind*; JPL Publication 96-17; Jet Propulsion Laboratory: Pasadena, CA, USA, 1996.
73. O'Driscoll, O.; Mouche, A.; Chapron, B.; Kleinherenbrink, M.; López-Dekker, P. Obukhov Length Estimation From Spaceborne Radars. *Geophys. Res. Lett.* **2023**, *50*, e2023GL104228. [CrossRef]
74. Bourassa, M.A.; Meissner, T.; Cerovecki, I.; Chang, P.S.; Dong, X.; Chiara, G.D.; Donlon, C.; Dukhovskoy, D.S.; Elya, J.; Fore, A.; et al. Remotely Sensed Winds and Wind Stresses for Marine Forecasting and Ocean Modeling. *Front. Mar. Sci.* **2019**, *6*, 443. [CrossRef]
75. Zanchetta, A.; Zecchetto, S. Wind direction retrieval from Sentinel-1 SAR images using ResNet. *Remote Sens. Environ.* **2021**, *253*, 112178. [CrossRef]